Supplementary Information (SI) for Journal of Materials Chemistry A.
This journal is © The Royal Society of Chemistry 2024

Electronic Supplementary Information

Second coordination sphere modulation during water oxidation with metal-hydroxide organic frameworks

Abhimanyu Yadav,[a,#] Toufik Ansari,[a,#] Pandian Mannu,[b] Baghendra Singh,[a] Ajit Kumar Singh,[a] Yu-Cheng Huang,[b] Vishal Kumar,[c] Sanjay Singh,[c] Chung-Li Dong,[,b] and Arindam Indra*[,a]*

[a]Department of Chemistry, IIT (BHU), Varanasi, UP-221005, India

E-mail: arindam.chy@iitbhu.ac.in

[b]Department of Physics, Tamkang, University, New Taipei City, Taiwan

E-mail cldong@mail.tku.edu.tw

[c]School of Materials Sciences and Technology, IIT (BHU), Varanasi, UP-221005, India

[#]Equally contributed to this work

Chemicals

All the chemicals (analytical grade) were utilized as purchased without any further purification. Nickel foam was procured from Axys Technology, West Bengal, India. Nickel(II) chloride hexahydrate ($NiCl_2 \cdot 6H_2O$) was procured from SDFCL. Iron(III) chloride ($FeCl_3$), dimethyl formamide (DMF), urea (NH_2CONH_2), potassium hydroxide (KOH), sodium hydroxide (NaOH) were procured from MERCK Life Sciences Pvt. Ltd. while ammonium fluoride (NH_4F) and chloranilic acid were purchased from SRL Pvt. Ltd and Sigma Aldrich, respectively. Sodium deuteroxide (NaOD) and deuterium oxide (D_2O) were purchased from ARMAR Isotopes, Germany. The catalyst synthesis, washing, and electrochemical measurements were carried out using double distilled water.

Instrumental

The PXRD patterns of the precatalysts and active catalysts were recorded in the 2-theta range of 5°-80°. The X-ray diffraction pattern (PXRD) was recorded on a Rigaku D/MAX RINT-2000 X-Ray diffractometer. The Cu-K_α (λ = 1.5418 Å) radiation was utilized for the PXRD measurements.

X-ray photoelectron spectroscopy (XPS) was carried out using VG/VG ESCA LAB 220i X-ray photoelectron spectrometer to determine the chemical nature, oxidation state, and surface structure of the synthesized catalysts. The XPS data were deconvoluted and analyzed using XPS 4.1 software.

The field emission EVO-Scanning Electron Microscope MA15/18 was utilized to investigate the morphology and surface characteristics of the catalysts. The energy dispersive X-ray (EDX) analysis was carried in Team Pegasus Integrated EDS-EBSD.

Tecnai G2 20 TWIN transmission electron microscope was used for the transmission electron microscopic (TEM) studies. A small piece of the catalyst film was sonicated in 2 mL ethanol for 1 h and the well-dispersed particles were drop cast on a TEM grid.

Atomic force microscopy (AFM) studies were conducted on NTEGRA Prima scanning probe microscope.

A Thermo Scientific Nicolet iS5 FTIR spectrometer was used to record IR spectra of the synthesized materials.

UV-Vis spectroscopic measurements were conducted using Cary 60 UV-Vis Spectrophotometer.

X-ray absorption spectroscopy

Synchrotron X-ray absorption near-edge structure (XANES) and the Extended X-ray absorption fine structure (EXAFS) at Ni K-edge were measured at beamline BL17C, which is equipped with a Si(111) double-crystal monochromator at Taiwan Light Source (TLS) of the National Synchrotron Radiation Research Center (NSRRC), Taiwan. The storage ring of TLS operates at 1.5 GeV with a current of about 360 mA. The spectra were collected in transmission mode. Ni foil used as the reference sample was measured simultaneously downstream so that energy calibration could be performed scan by scan. Raw data were analysed following standard procedures, including pre-edge and post-edge background subtractions, normalization with respect to the edge jump, and Fourier transformation. Ni L-edge, Fe L-edge, and O K-edge measurements were performed at beamline BL20A using total electron yield mode. The energy resolutions of hard XAS (Ni K-edge and Fe K-edge) and soft XAS (Ni L-edge, Fe L-edge and O K-edge) were set to 0.3 and 0.1 eV, respectively.

Experimental Section

Activation of nickel foam (NF)

The pieces of nickel foams (1 × 2 cm^2) were cleaned with acetone and water. Further, the pieces of nickel foam were treated with 1.0 M HCl for 15 min under ultra-sonication conditions to remove the surface impurities. The

freshly activated NF was utilized for the synthesis of the catalysts.

Synthesis of nickel-iron layered double hydroxide on nickel foam (NiFe-LDH@NF)

$NiCl_2 \cdot 6H_2O$ (1.0 mmol), $FeCl_3$ (1.0 mmol), NH_4F (4.0 mmol), and NH_2CONH_2 (10.0 mmol) were dissolved in 12 mL water and stirred for 30 min. The pieces of nickel foam were placed vertically inside the solution in Teflon lined autoclave and sealed. The autoclave was heated at 120 °C for 5 h. After normal cooling to the room temperature, the films of NiFe-LDH@NF were washed with water followed by ethanol and dried in an air oven at 50 °C for 12 h.

The $Ni(OH)_2$@NF films were prepared using a similar method to NiFe-LDH@NF by taking only $NiCl_2 \cdot 6H_2O$ as the metal source (2.0 mmol).

Synthesis of NiFe-HOF@NF

For the synthesis of NiFe-HOF@NF, 32 mg of chloranilic acid was dissolved in 10 mL of mixed solution of DMF and water (10:1). Two pieces of NiFe-LDH@NF were immersed vertically into the solution in a Teflon lined autoclave. The autoclave was sealed and placed in a preheated air oven at 100 °C for 6 h. After the normal cooling, as synthesized NiFe-HOF@NF films were washed with DMF and ethanol for several times. The films were further dried in an air oven at 50 °C for overnight.

For the comparison purpose, Ni-HOF@NF was also synthesized using a similar method by immersing $Ni(OH)_2$@NF into the solution of chloranilic acid.

Table S1. Details of the precatalysts and active catalysts

Sr. No.	Precatalyst	No. of CV-cycles for activation	Active catalyst
1	Ni-HOF	54	AC-1
2	NiFe-HOF	40	AC-2
3	NiFe-LDH	40	AC-3

Electrochemical measurements

The electrochemical measurements were carried out in a single-compartment three-electrode electrochemical cell in 1.0 M aqueous KOH solution. The HOF films on nickel foam was employed as the working electrode and Pt wire was utilized as the counter electrode. The Hg/HgO electrode was utilized as the reference electrode in 1.0 M aqueous KOH solution (pH 13.7). Linear sweep voltammetry (LSV) were performed and presented with 70% *iR* compensation. All the potentials were presented against reversible hydrogen electrode (RHE) using the formula:

$E_{RHE} = E_{Hg/HgO} + 0.098 + 0.059pH$

Electrochemical impedance spectroscopic (EIS) measurements were recorded in the frequency range from 0.001 to 100,000 Hz and amplitude of 10 mV. The charge transfer resistance (R_{ct}) was calculated from the diameter of the semicircle in the Nyquist plots.

The chronoamperometric measurements (CA) were carried out in 1.0 M aqueous KOH at a constant potentials and represented without *iR* compensation. Tafel plots were determined by potentiostatic measurements at the potentials where current density reached up to 10 mA cm^{-2}. The Tafel slope was calculated using Tafel equation:

$$\eta = b \log j + a$$

Where, η denotes the overpotential (V), j is the current density (A cm^{-2}), and b is the Tafel slope (V dec^{-1}).

For C_{dl} measurements, CV was carried out at a potential range, where no faradaic process occurred.

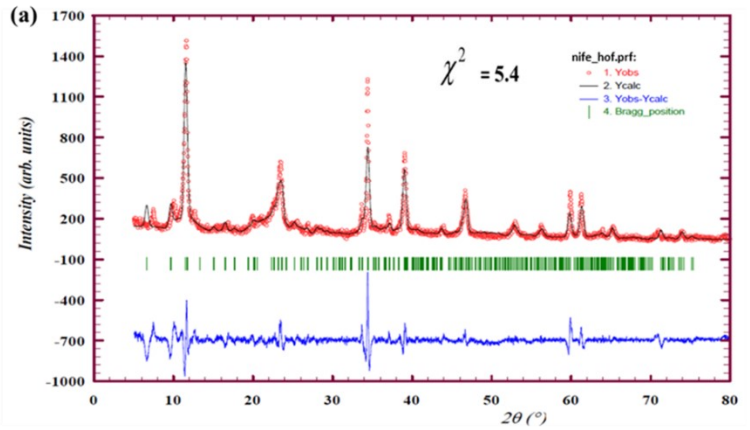

(b)	
crystal system	Trigonal
space group	$P\bar{3}1_m$
a=b, Å	15.328401
c, Å	9.1421213
α, deg	90
β, deg	90
γ, deg	120
V, Å	1860.2439

Figure S1. Simulated PXRD patterns of (a) NiFe-HOF@NF and (b) crystal structure data of NiFe-HOF@NF.[1,2]

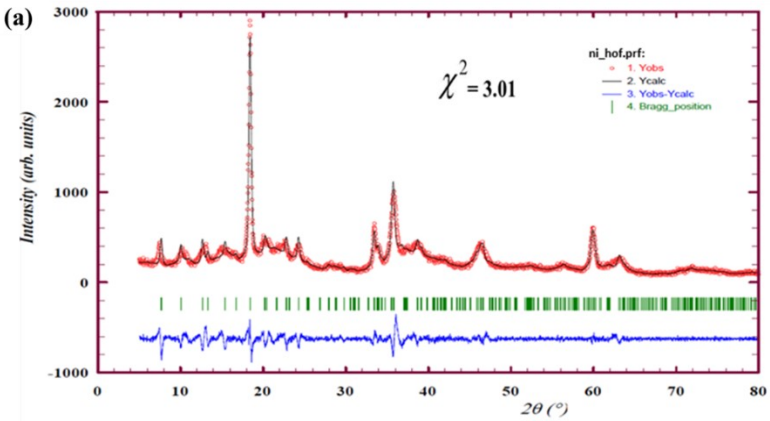

(b)	
crystal system	Trigonal
space group	$P\bar{3}1_m$
a=b, Å	13.2824
c, Å	8.7814
α, deg	90
β, deg	90
γ, deg	120
V, Å	1341.6813

Figure S2. Simulated PXRD patterns of (a) Ni-HOF@NF; (b) crystal structure data of Ni-HOF@NF.[1,2]

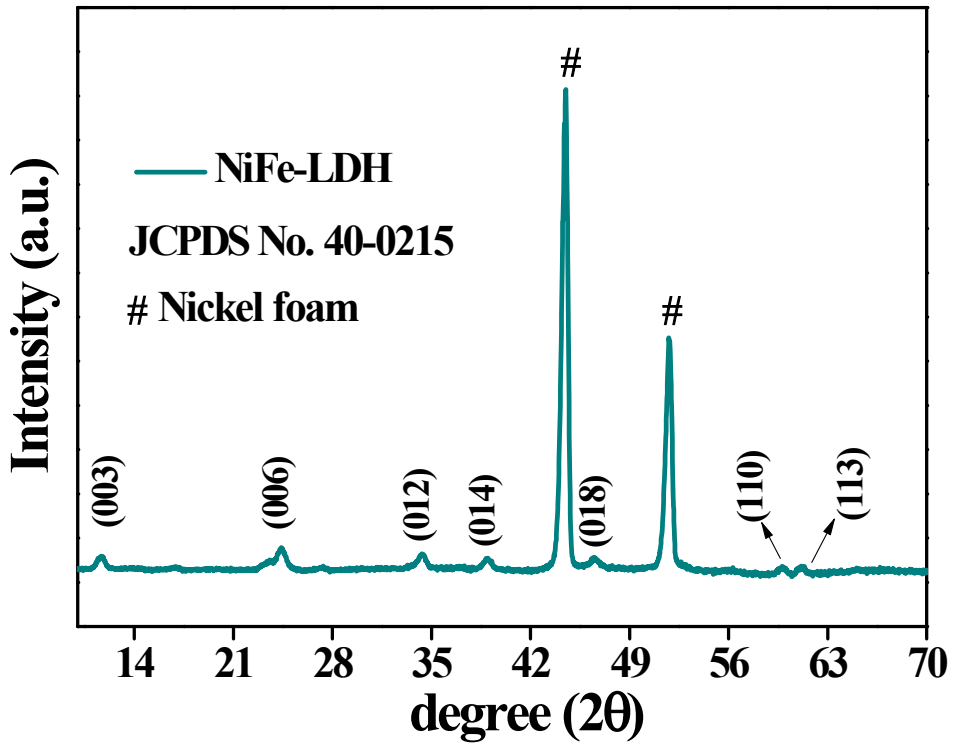

Figure S3. PXRD pattern of NiFe-LDH. All the peaks are well matched with JCPDS No. 40-0215.

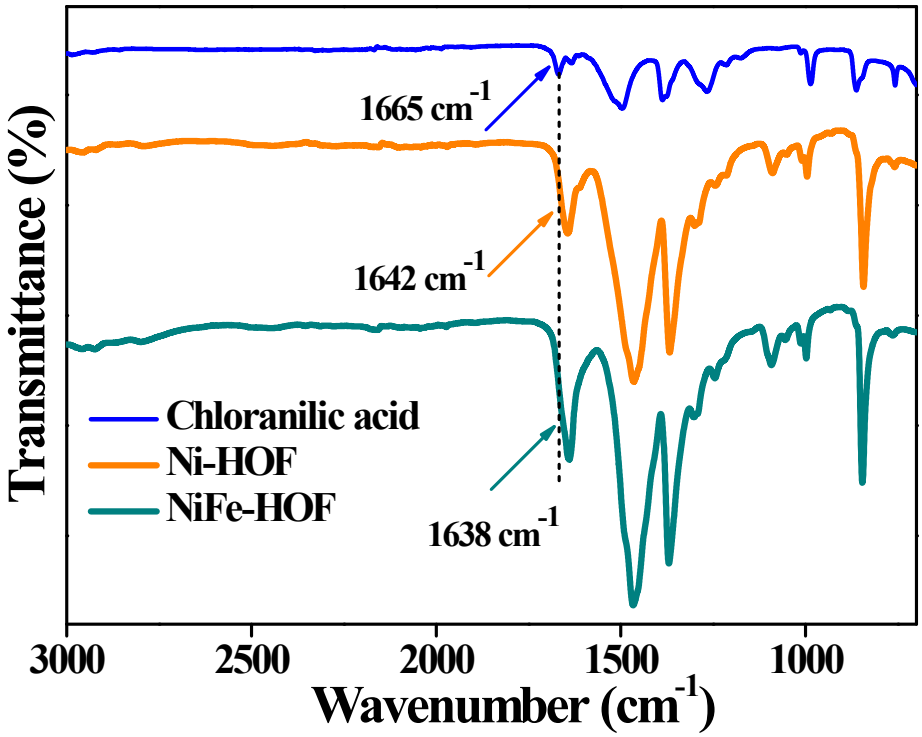

Figure S4. IR spectra of NiFe-HOF@NF, Ni-HOF@NF, and free chloranilic acid. The peaks at 1638 cm^{-1}, 1643 cm^{-1}, and 1665 cm^{-1} were assigned to the stretching vibrations of C=O group NiFe-HOF@NF, Ni-HOF@NF, and free chloranilic acid, respectively. The red shifts of the C=O vibrations, relative to the peaks of free chloranilic acid was observed due to the delocalization of the π-electrons in the bidentate chloranilate anion coordinated to metal center.[2,3,4,5]

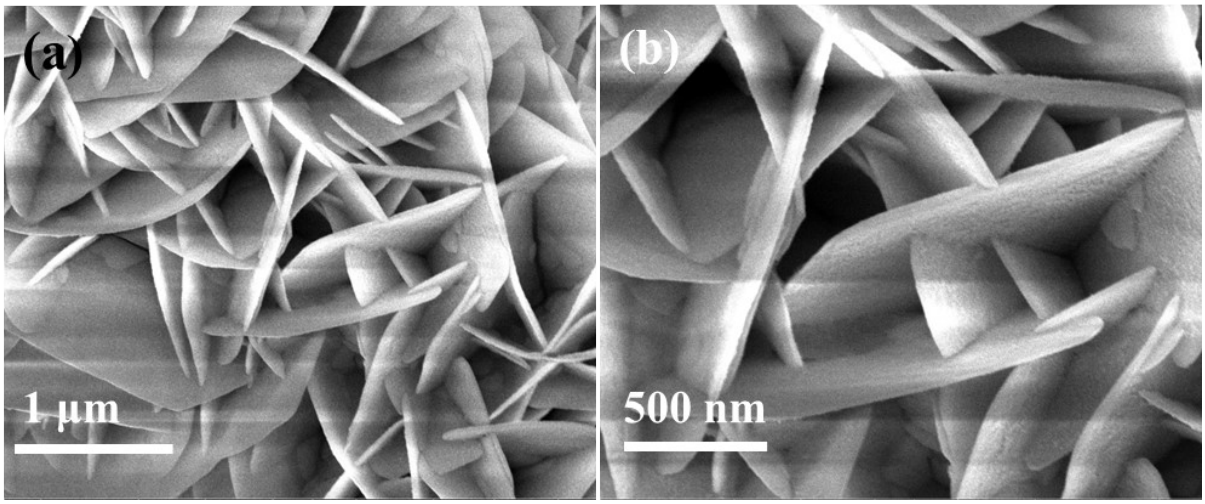

Figure S5. (a-b) FESEM images of NiFe-LDH showing the nano plate like morphology.

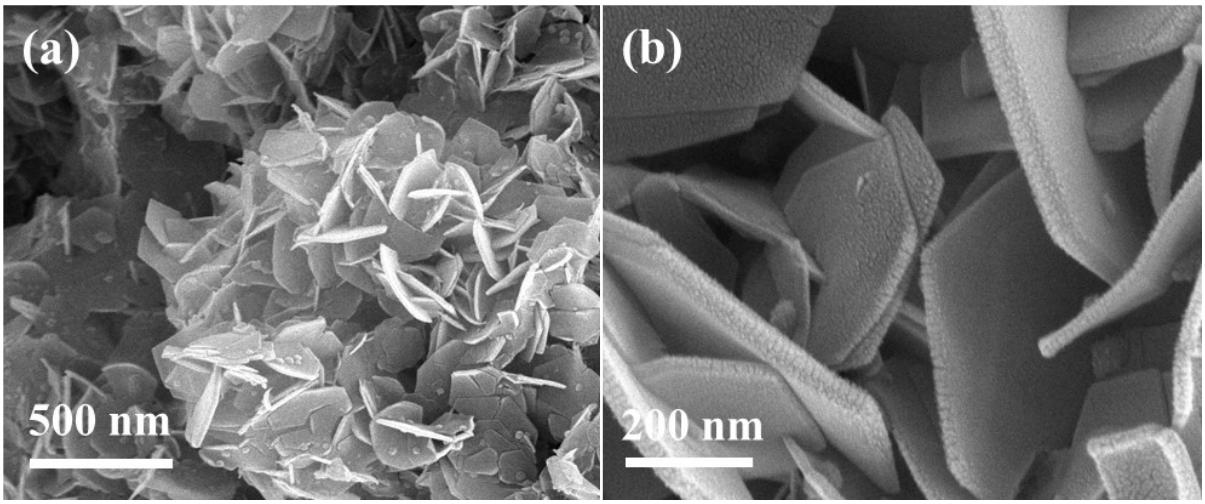

Figure S6. (a-b) FESEM images of Ni-HOF@NF showing the hexagonal plate like morphology.

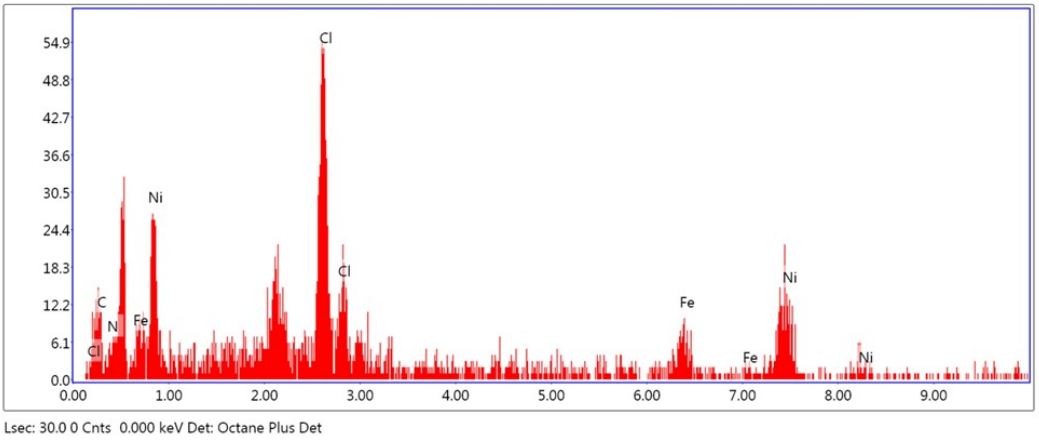

Figure S7. EDX spectrum of NiFe-HOF indicating the presence of the elements Ni, Fe, C, N, Cl, and O.

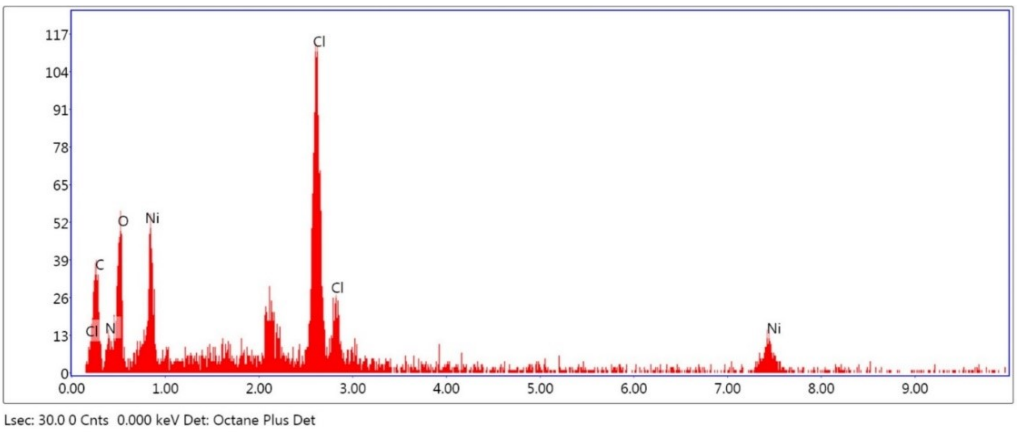

Figure S8. EDX spectrum of Ni-HOF indicating the presence of the elements Ni, C, N, Cl, and O.

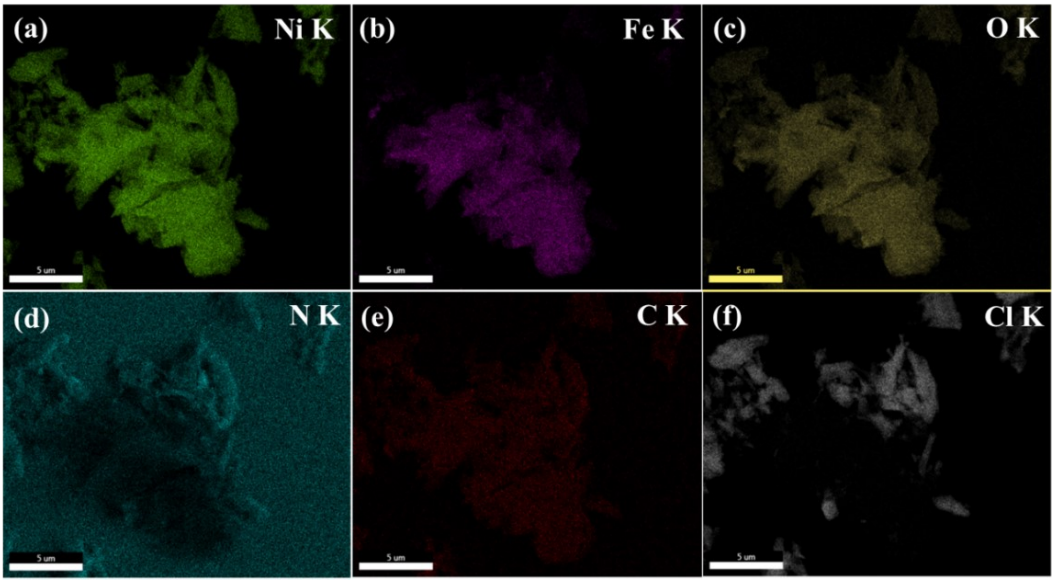

Figure S9. Elemental mapping images of NiFe-HOF@NF, (a) Ni K, (b) Fe K, (c) O K, (d) N K, (e) C K and (f) Cl K.

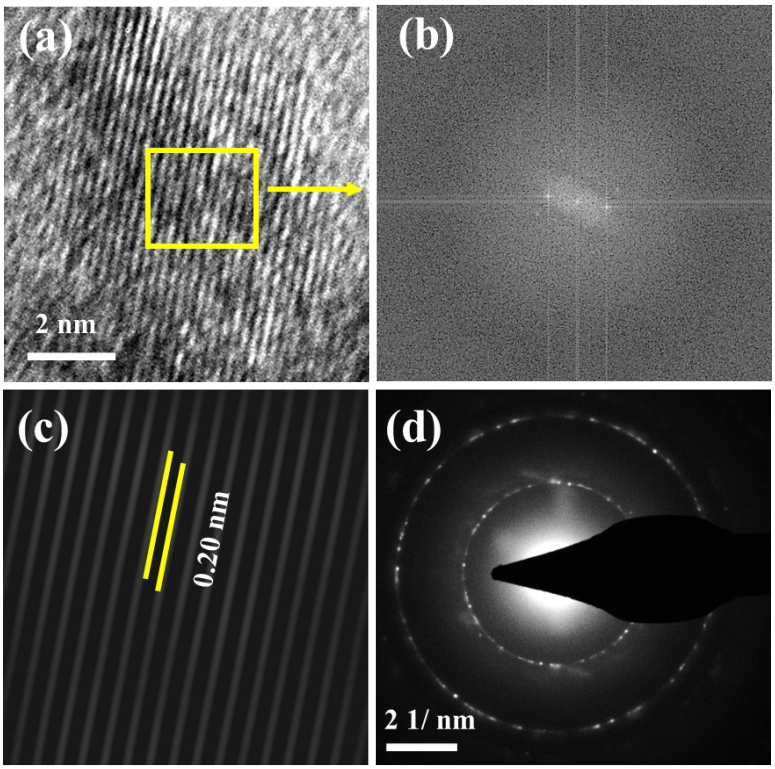

Figure S10. (a) HRTEM image of NiFe-HOF; (b) FFT of the selected area in the figure (a); (c) inverse FFT of figure (b); (d) SAED pattern of NiFe-HOF.

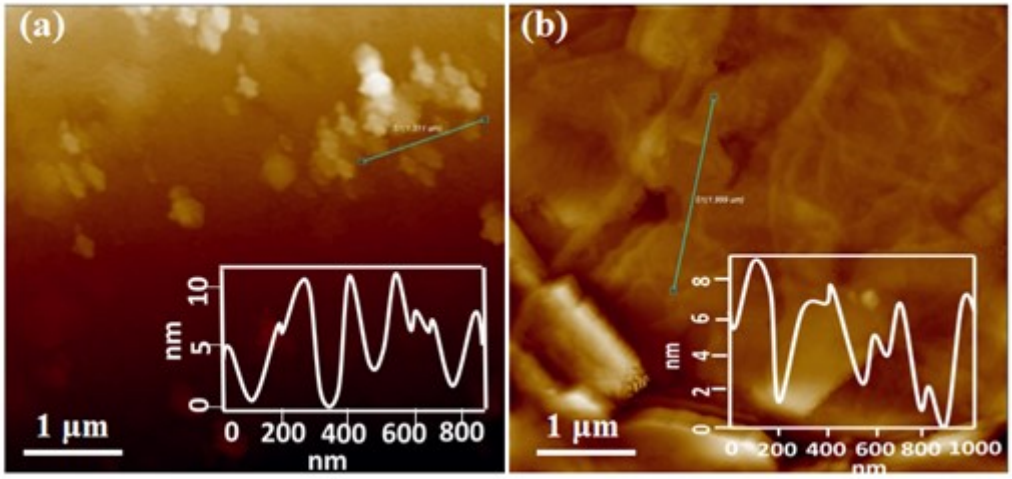

Figure S11. (a) AFM image of Ni-HOF showing the 8-11 nm thickness of the nanoplates (height profile inset), (b) AFM image of NiFe-HOF showing the 6-9 nm thickness of the nanoplates (height profile inset).

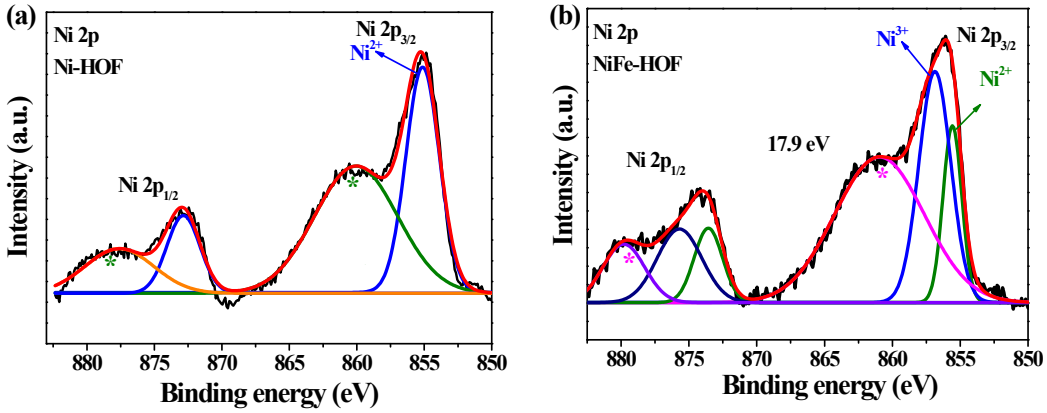

Figure S12. (a) Ni 2p-XPS of Ni-HOF@NF showing two peaks at 855.23 eV and 872.91 eV corresponding to the Ni $2p_{3/2}$ and Ni $2p_{1/2}$, respectively. The peak at 855.08 eV was assigned for the Ni^{2+} whereas the * marked peaks were attributed to the satellite peaks; (b) Ni 2p-XPS of NiFe-HOF@NF indicating the two peaks at 856.01 eV and 873.91 eV corresponding to the Ni $2p_{3/2}$ and Ni $2p_{1/2}$, respectively, the peaks at 856.01 eV and 856. 91 eV were assigned for the Ni^{2+} and Ni^{3+} species, respectively, while the * marked peaks were observed for satellite peaks of Ni^{2+}.[1,6]

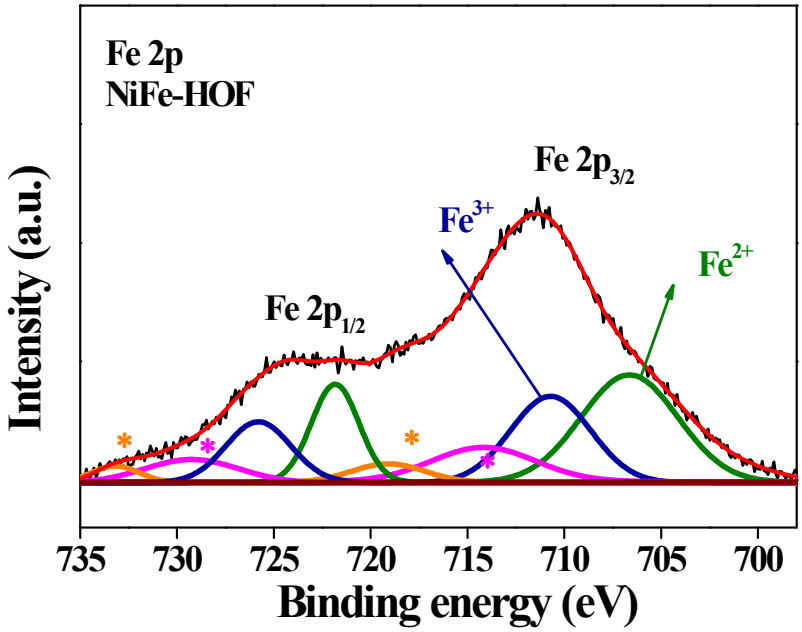

Figure S13. Fe 2p-XPS of NiFe-HOF@NF showing two peaks at 711.12 eV and 725.21 eV corresponding to the Fe $2p_{3/2}$ and Fe $2p_{1/2}$, respectively. The peaks at 706.28 eV and 711.12 eV were assigned to the Fe^{2+} and Fe^{3+} species. The peaks marked with * are attributed to satellite peaks of Fe^{2+} (pink) and Fe^{3+} (orange), respectively [7,8,9,10]

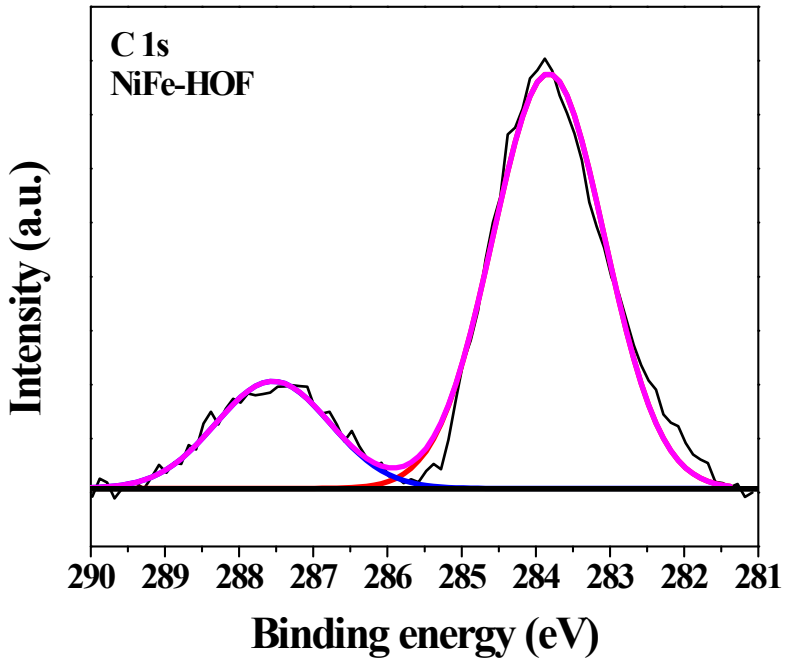

Figure S14. C 1s-XPS of NiFe-HOF@NF showing two peaks at binding energies 287.32 eV and 283.67 eV. The peaks at 287.32 eV and 283.67 eV were assigned to the C-N and C=O bond, respectively.[7]

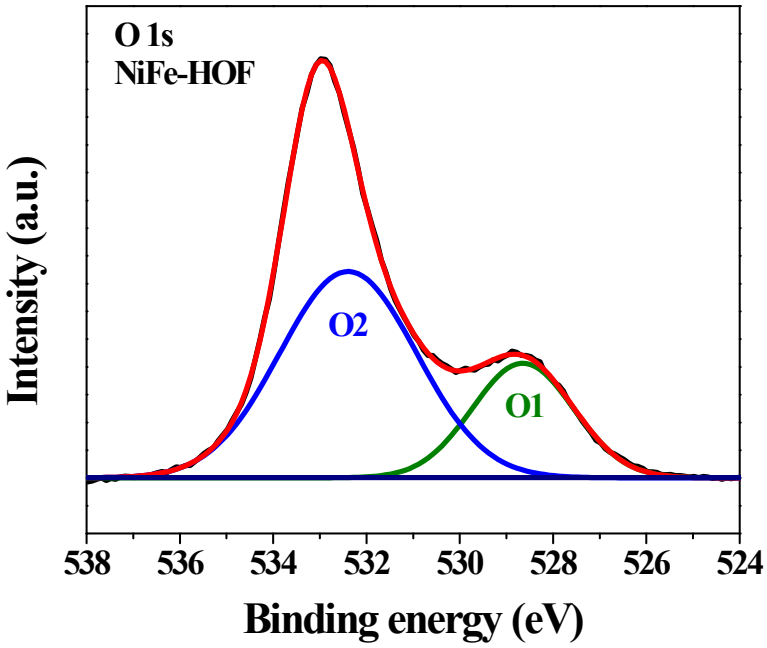

Figure S15. O 1s-XPS of NiFe-HOF@NF showing three peaks at 528.61 eV (O1) and 532.41 eV (O2). The peaks at 528.61 eV (O1) and 532.41 eV (O2) were assigned for the metal-oxygen bond and surface –OH groups, respectively.[8,9,10,11,12]

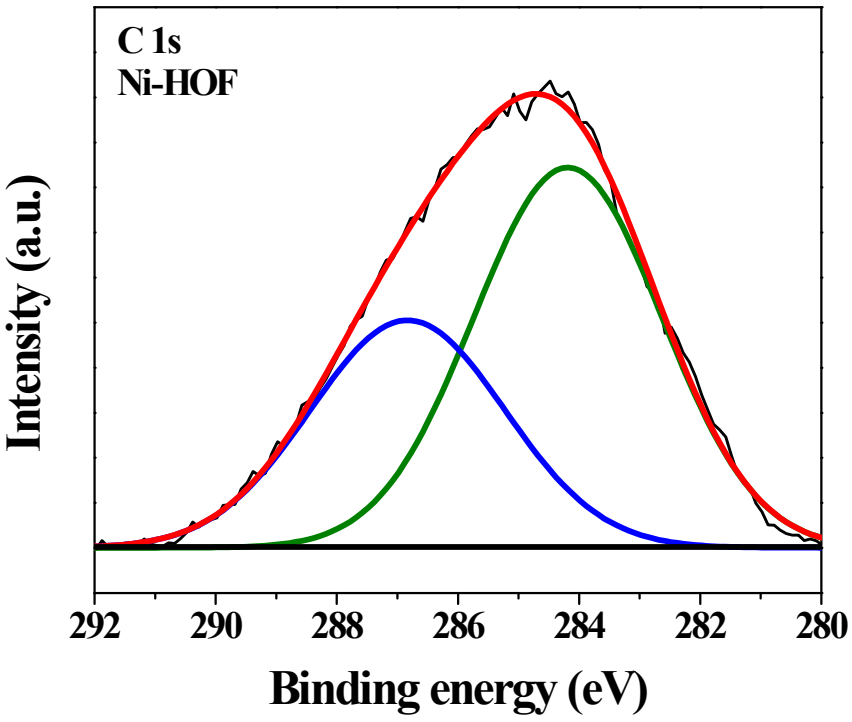

Figure S16. C 1s-XPS of Ni-HOF@NF showing two peaks at 284.91 eV and 286.63 eV. The peaks at 284.91 eV and 286.63 eV were assigned for the C=C and C-O bond, respectively.[9,10,11]

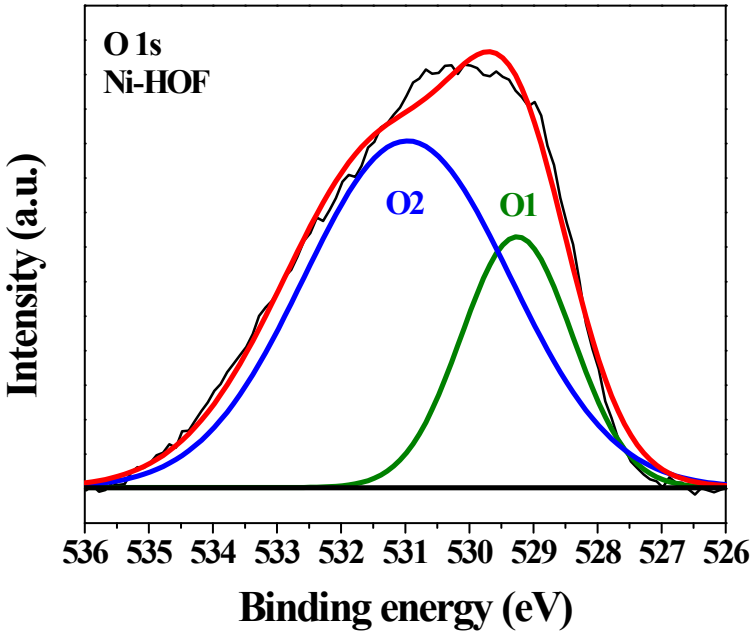

Figure S17. O 1s-XPS of Ni-HOF@NF showing three peaks at 529.30 eV (O1) and 530.97 eV (O2). The peaks at 529.30 eV (O1) and 530.97 eV (O2) were assigned for the metal-oxygen bond and surface –OH group, respectively.[11,12]

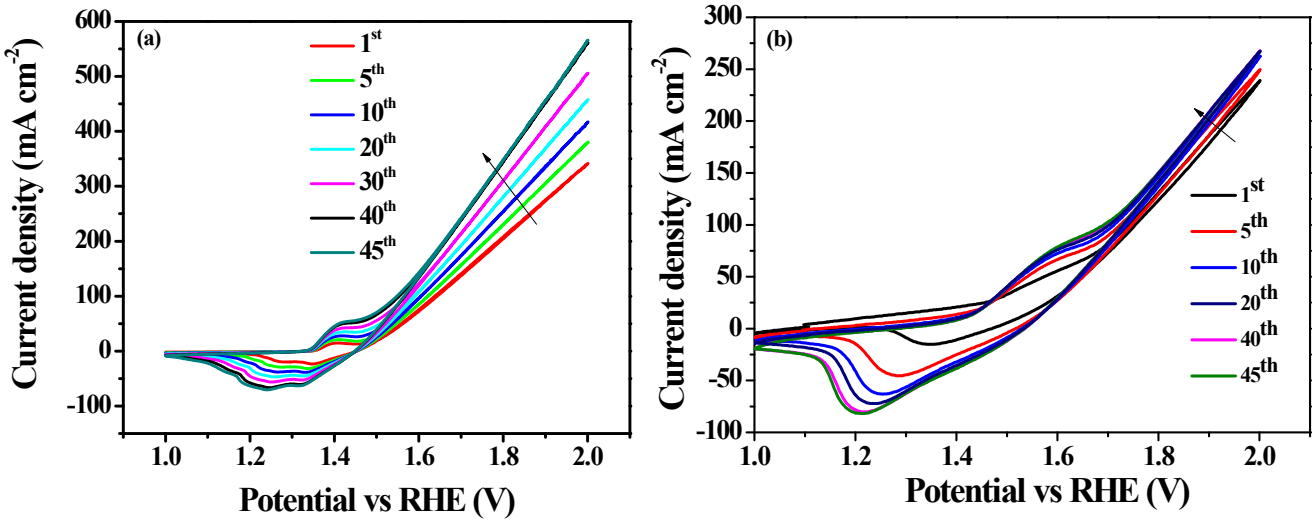

Figure S18. (a) CV profiles for the electrochemical activation of NiFe-HOF@NF in 1.0 M KOH solution under applied anodic potential indicating the electrochemical reconstruction of the precatalyst to active catalyst in 40 CV cycles (scan rate 20 mV s^{-1}) and (b) CV profiles for the electrochemical activation of NiFe-LDH@NF in 1.0 M KOH solution under applied anodic potential requires 40 CV cycles with a scan rate of 20 mV s^{-1}.

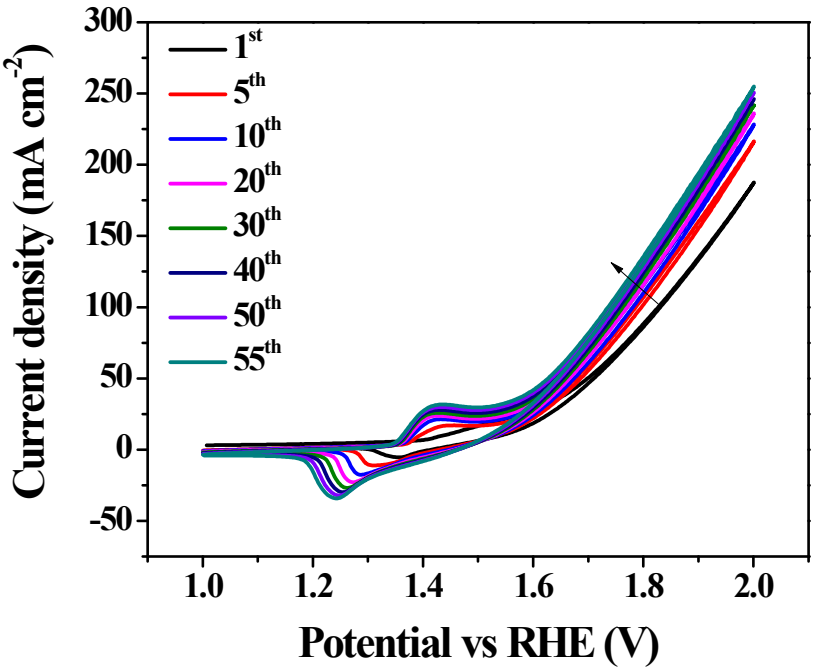

Figure S19. CV profiles for the electrochemical activation of Ni-HOF@NF in 1.0 M KOH solution under applied anodic potential indicating the electrochemical reconstruction of the precatalyst to active catalyst in 54 CV cycles (Scan rate 20 mV s^{-1}).

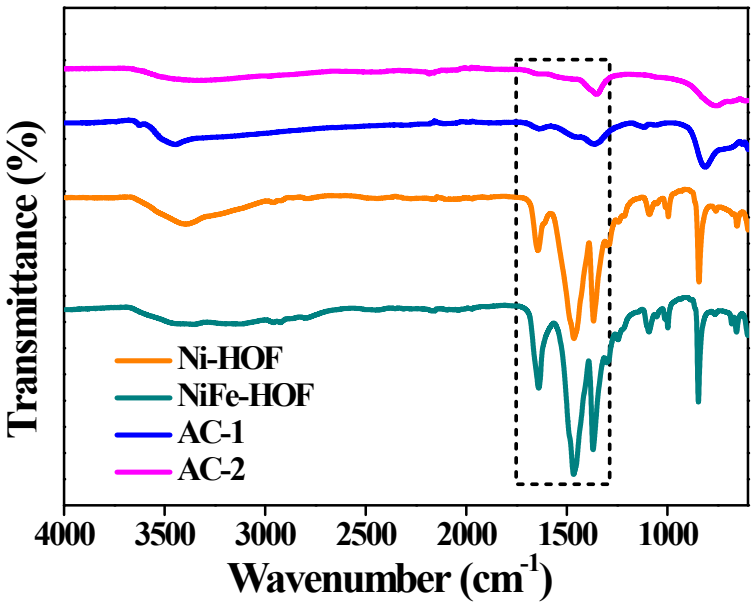

Figure S20. IR spectra of NiFe-HOF and Ni-HOF and corresponding active catalyst AC-2 and AC-1 showing that the peaks for C=O and C-O vibrations were disappeared after electrochemical activation. The peaks for stretching and bending vibrations of water molecules were originated after the activation.[8,9]

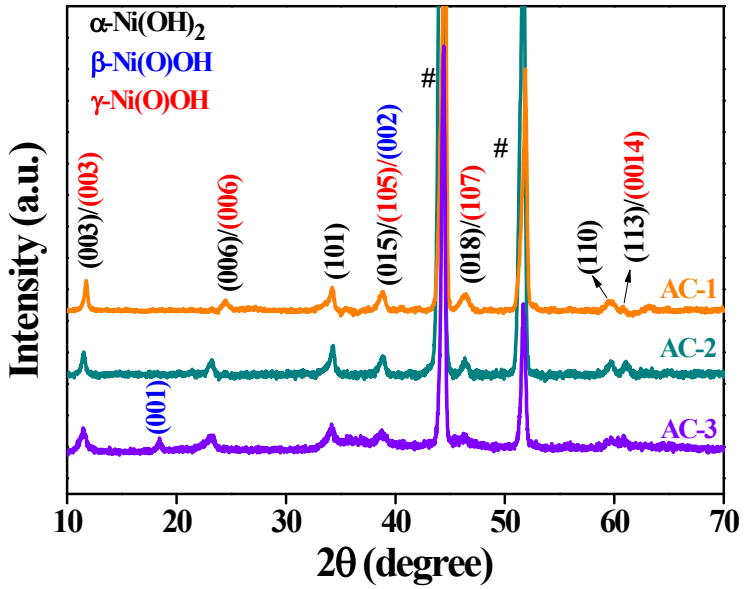

Figure S21. PXRD patterns of the active catalysts AC-1 and AC-2 and AC-3. The peaks are well matched with the α-$Ni(OH)_2$ (JCPDF No: 38-0175), γ-Ni(O)OH (JCPDF No: 06-0075) for AC-1 and AC-2 and α-$Ni(OH)_2$ (JCPDF No: 38-0175), β-Ni(O)OH (JCPDF No: 06-0141) for AC-3. A negative shift of 0.23° in two theta value for (003) peak was observed for AC-2 compared to AC-1 due to the inter-layer expansion.

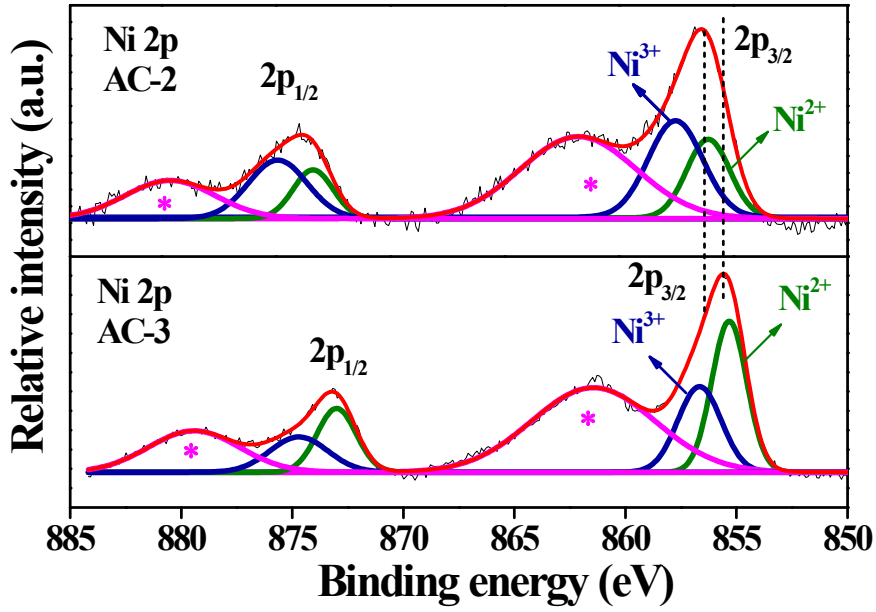

Figure S22. Ni 2p XPS of AC-3 and AC-2 showing the peaks for Ni $2p_{3/2}$ and Ni $2p_{1/2}$. In AC-3, the peaks at 855.51 eV and 856.79 eV corresponds to Ni^{2+} and Ni^{3+}, respectively. In contrast, AC-2 shows the Ni^{2+} peak at 856.12 eV and the Ni^{3+} peak at 857.41 eV. The positive shift of the Ni $2p_{3/2}$ peak in AC-2 (by 0.85 eV) suggests the presence of high valence Ni. The peaks marked with * are attributed to satellite peaks.[1,6]

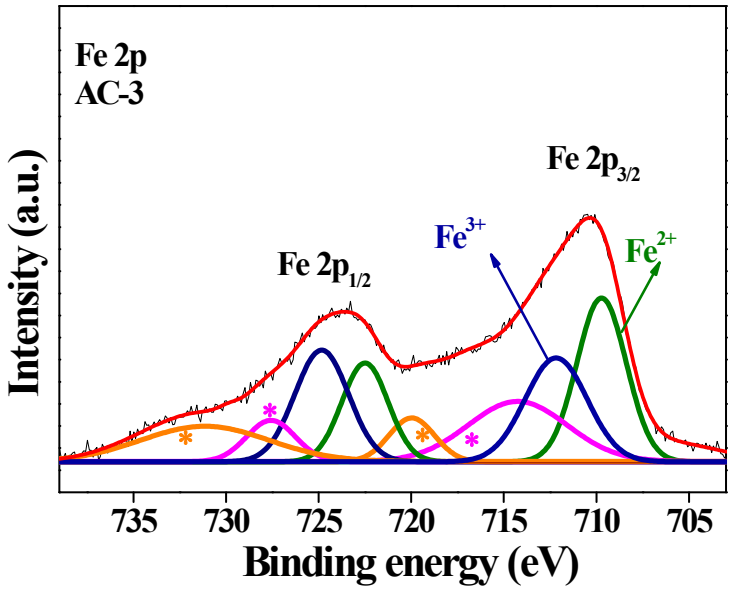

Figure S23. Fe 2p-XPS of AC-3 showing two peaks at 710.05 eV and 724.10 eV corresponding to the Fe $2p_{3/2}$ and Fe $2p_{1/2}$, respectively. The peaks at 709.28 eV and 711.50 eV were assigned for the Fe^{2+} and Fe^{3+}, respectively. The peaks marked with ∗ are attributed to satellite peaks of Fe^{2+} (pink) and Fe^{3+} (orange) respectively.[7,8,9,10]

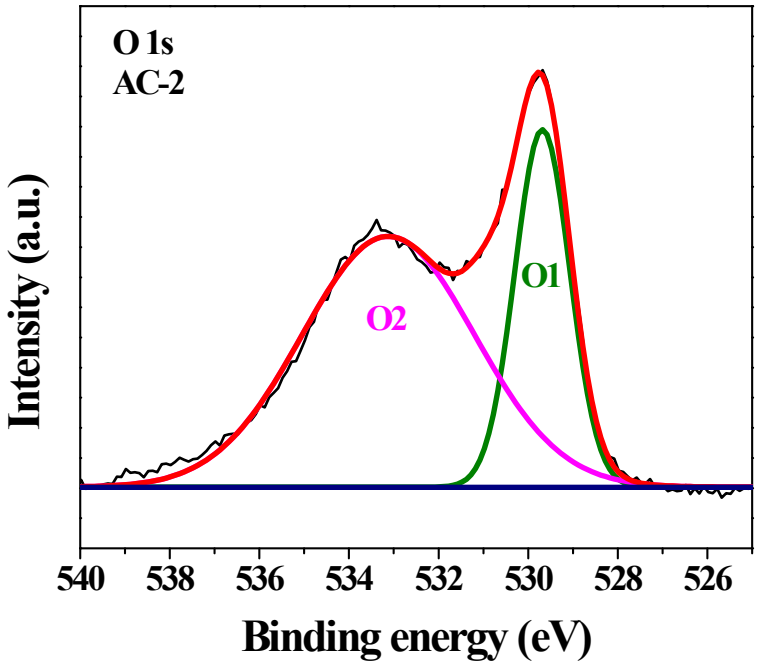

Figure S24. O 1s-XPS of AC-2 showing two peaks at 529.71 eV (O1) and 533.12 eV (O2) assigned for metal-oxygen (M-O) bond and adsorbed water molecules, respectively.[8,11,13,14]

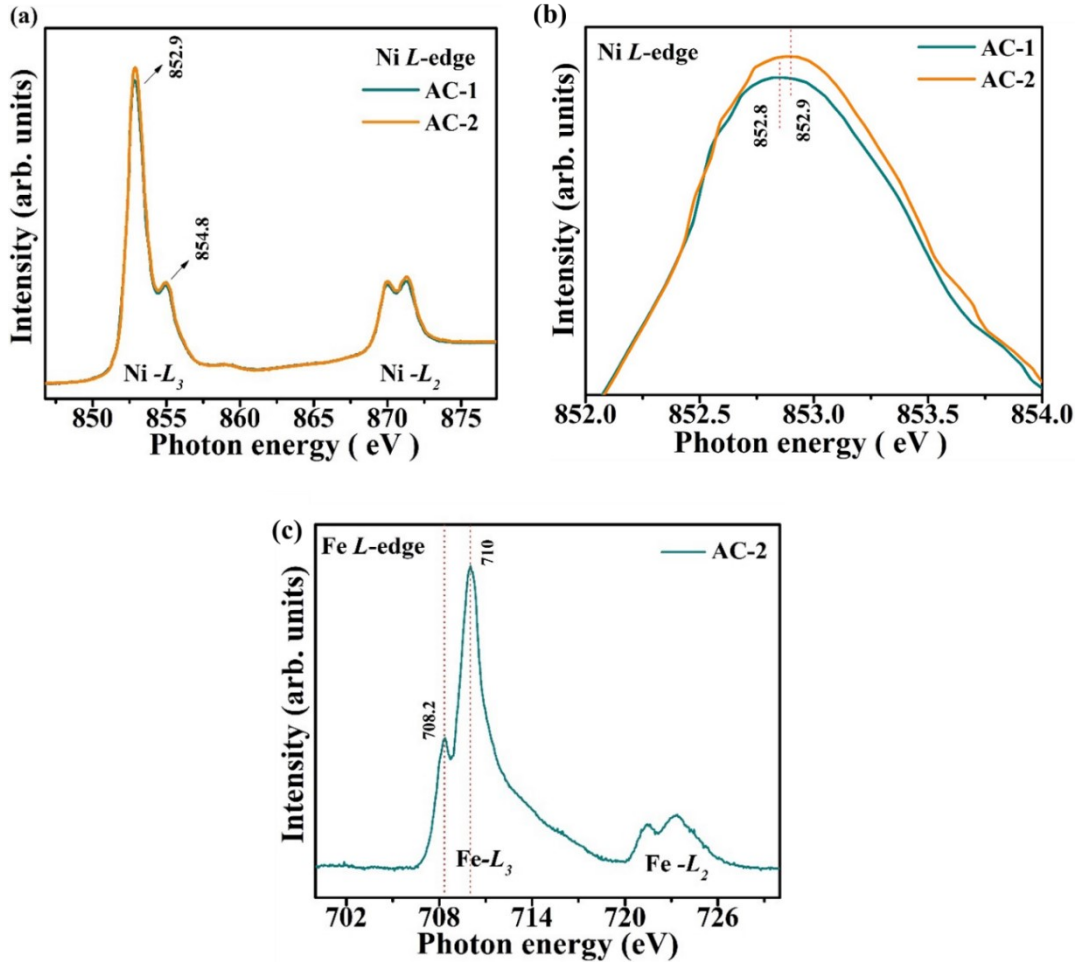

Figure S25. (a) Ni $L_{3,2}$ -edge XAS spectra of AC-1 and AC-2; (b) comparison of magnified Ni L-edge XAS spectra and (c) Fe $L_{3,2}$-edge XAS spectra of AC-2.[15,16,17]

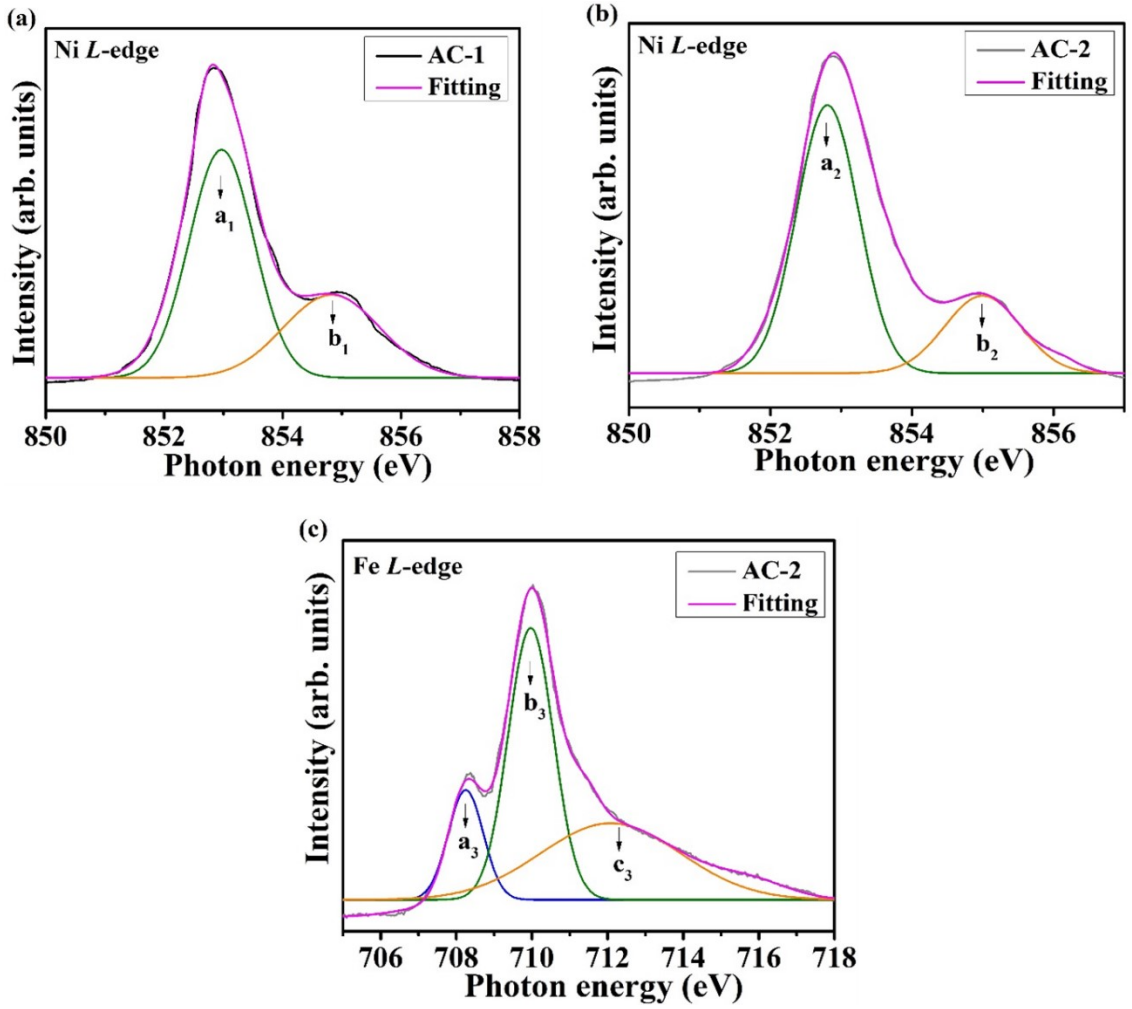

Figure S26. Curve fitting of Ni L-edge XAS spectra of (a) AC-1; (b) AC-2; (c) Fe $L_{3,2}$-edge XAS spectra of AC-2.[15,16,17]

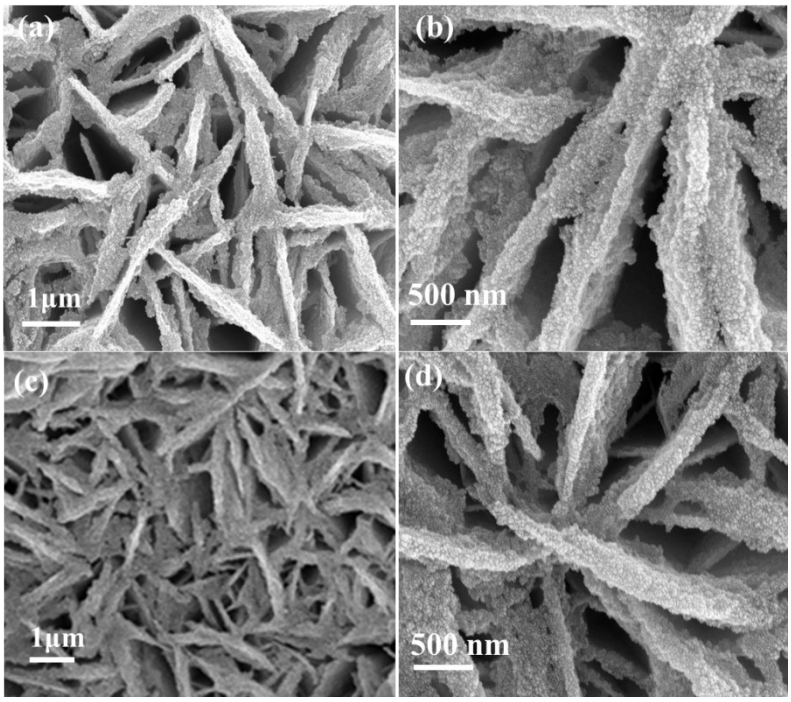

Figure S27. (a-b) FESEM images of the active catalyst AC-2 and (c-d) FESEM images of the active catalyst AC-1 showing the nanosheets.

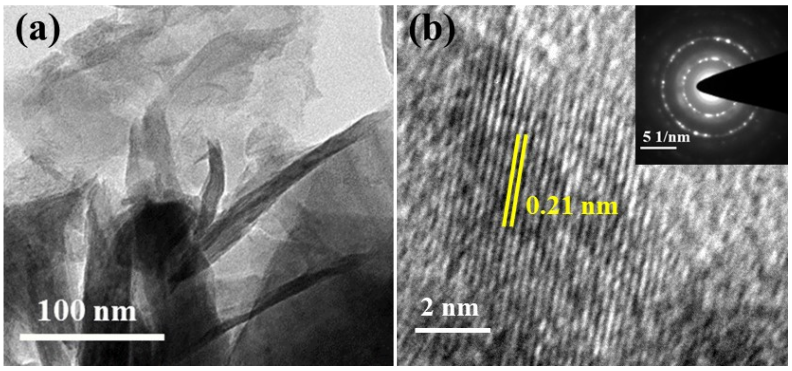

Figure S28. (a) TEM image of the active catalyst AC-1 showing the nanosheet morphology and (b) HRTEM image of the active catalyst AC-1 indicating the lattice spacing of 0.21 nm assigned for the (105) plane of γ-Ni(O)OH (JCPDF No: 06-0075) (SAED inset).

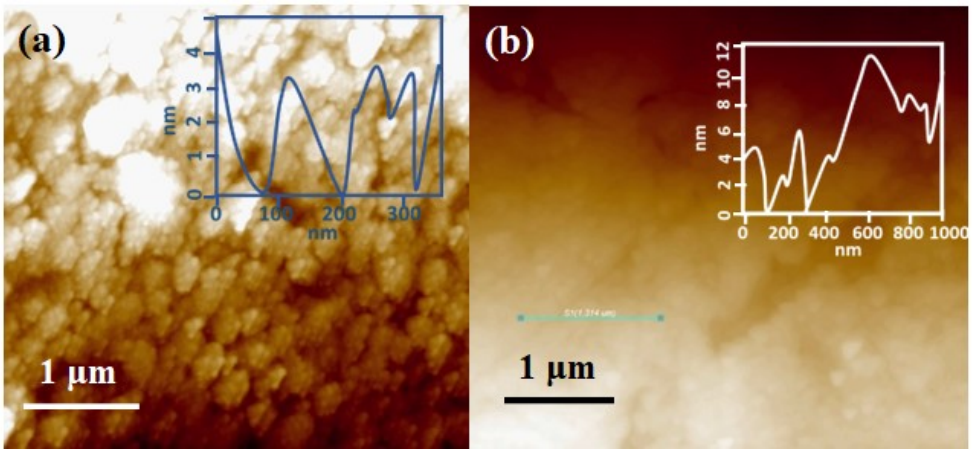

Figure S29. (a) AFM image of the active catalyst AC-2 showing the ultrathin nanosheets with ~3-4 nm thickness (inset height profile) and (b) AFM image of the active catalyst AC-1 showing the ultrathin nanosheets with ~6-11 nm thickness (inset height profile).

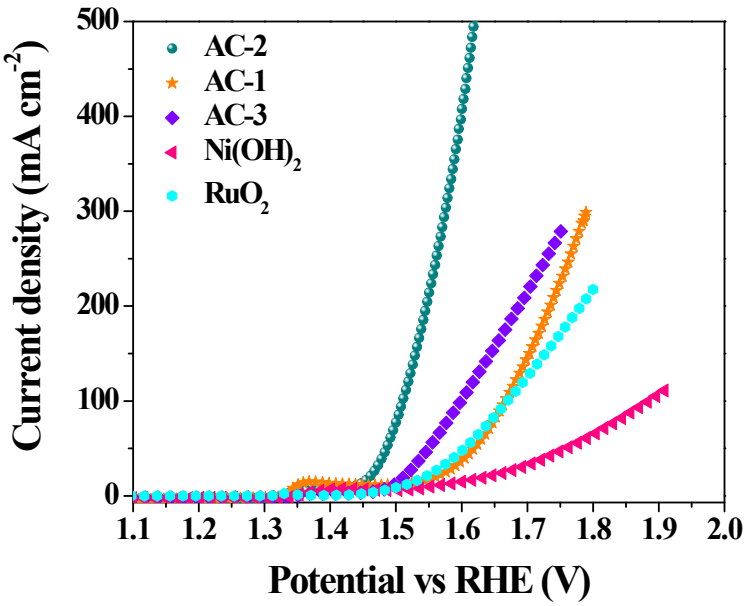

Figure S30. LSV profiles for the oxygen evolution reaction of AC-2 and AC-1 compared with AC-3, $Ni(OH)_2$ and RuO_2 showing the best OER activity for AC-2.

Table S2. Comparison of the oxygen evolution activity of AC-2 with literature reported MOF-derived catalysts, layered double hydroxides and self-supported catalysts.

Catalyst	Electrolyte	Current density (mA/cm^2)	Overpotential (mV)	References
(a) This work				
AC-2	**1.0 M aqueous KOH**	**50**	**254**	**This work**
AC-1	**1.0 M aqueous KOH**	**50**	**316**	**This work**
(b) MOF-derived catalysts				
$NiCoO_x$	1.0 M aqueous KOH	10	380	18
NiFeP	1.0 M aqueous KOH	10	290	19
$NiCoSe_2$	1.0 M aqueous KOH	10	320	20
NiCo-Oxide	1.0 M aqueous KOH	10	280	21
NiFe@C	1.0 M aqueous KOH	10	280	22
Ni_xP_y	1.0 M aqueous KOH	10	300	23
NiCoFeS	1.0 M aqueous KOH	10	320	24
(c) Self-supported catalysts				
NiO@NF	1.0 M aqueous KOH	10	422	25
NiP@NF	1.0 M aqueous KOH	10	335	26
NiO@NF	1.0 M aqueous KOH	10	390	27
$(Ni,Co)_{0.85}Se$@CC	1.0 M aqueous KOH	10	300	28
NiFeSe@NiSe/O@CC	1.0 M aqueous KOH	10	270	29
NiSe@NiOOH@NF	1.0 M aqueous KOH	50	332	30
(d) Ultrathin layered double hydroxide nanosheets				
NiFeCo-LDH@CuO	1.0 M aqueous KOH	10	249	31
NiFe-LDH	1.0 M aqueous KOH	50	290	32
NiFe-LDH	1.0 M aqueous KOH	50	280	33
NiFeV-LDH	1.0 M aqueous KOH	20	260	34
NiFe-LDH	1.0 M aqueous KOH	50	325	35
NiFe-LDH	1.0 M aqueous KOH	10	247	36

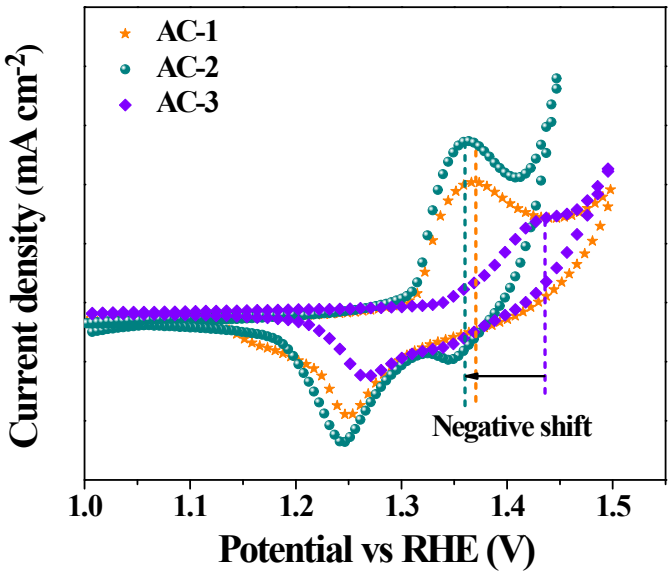

Figure S31. CV profiles during the oxygen evolution reaction with AC-1, AC-2, and AC-3 showed the shifting of the Ni^{2+}/Ni^{3+} redox peak. The negative shift of the Ni^{2+}/Ni^{3+} oxidation peak in AC-2 confirmed the formation of Ni^{3+} at lower potential in AC-2 resulting in the improved OER activity.[37]

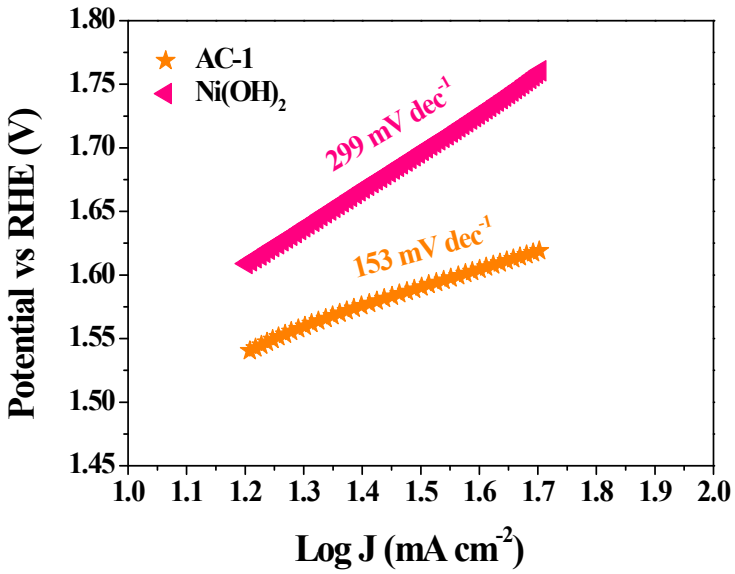

Figure S32. Tafel plots of AC-1 compared with $Ni(OH)_2$ showing the lower Tafel slope for AC-1.

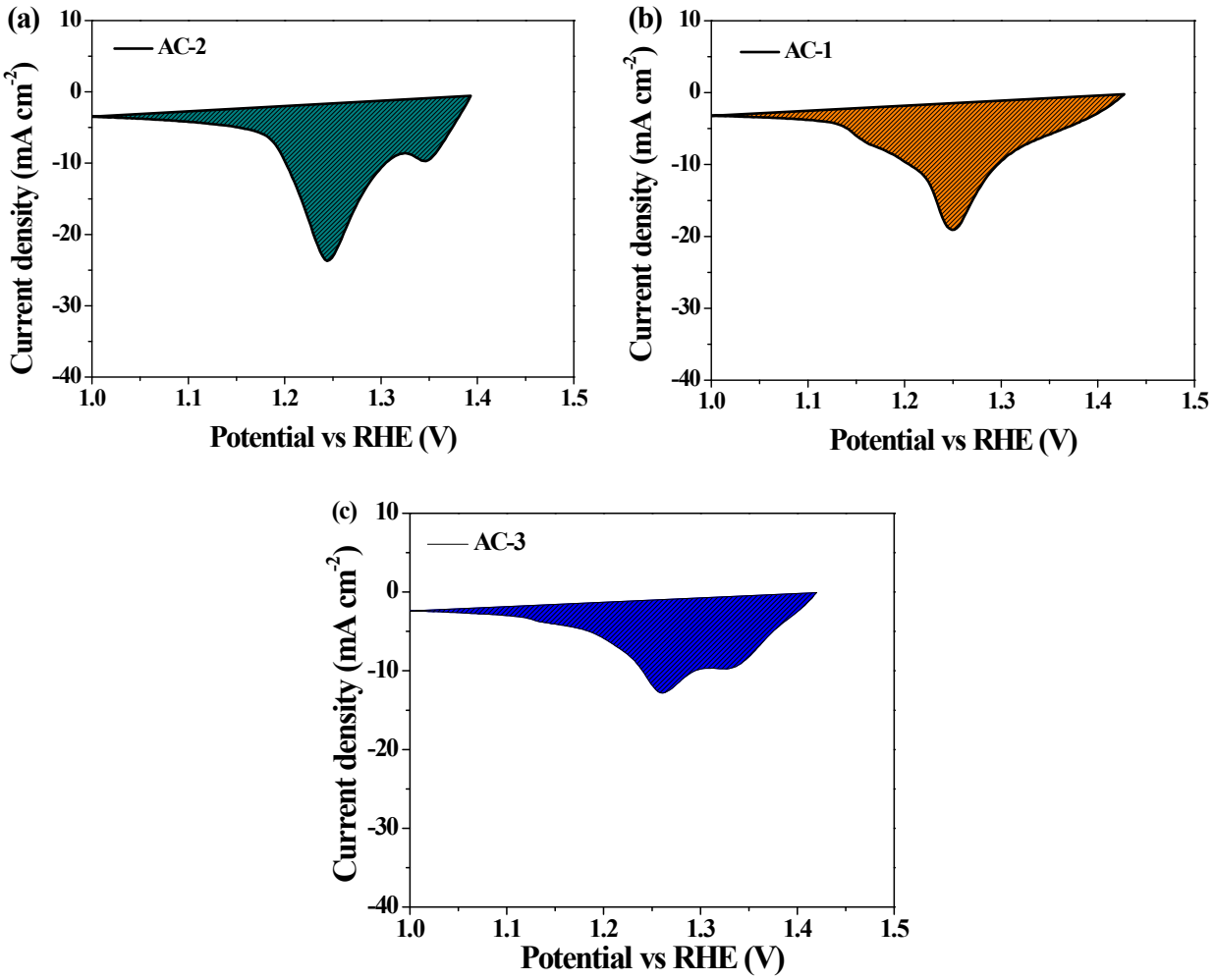

Figure S33. Reduction peak area of (a) AC-2; (b) AC-1, and (c) AC-3 utilized for integration to determine the number of surface-active sites.[38,39]

Equation S1: Determination of surface-active sites using area integration of the reduction peak.

For AC-2

Calculated area associated with the reduction peak = 2.4648×10^{-3} V A

Hence the associated charge is = 2.4648×10^{-3} V A / 0.005 V s^{-1}

$= 492.96 \times 10^{-3}$ A s

$= 492.96 \times 10^{-3}$ C

Now, the number of electron transferred is = 492.96×10^{-3} C / 1.602×10^{-19} C

$= 3.07 \times 10^{18}$

Since the reduction of Ni^{3+} to Ni^{2+} is a single electron transfer reaction, the number of electrons calculated above is the same as the number of surface-active sites.

Hence,

The surface-active Ni^{3+} sites participated in OER is = $\mathbf{3.07 \times 10^{18}}$

For AC-1

Calculated area associated with the reduction peak = 2.2359×10^{-3} V A

Hence the associated charge is = 2.2359×10^{-3} V A / 0.005 V s^{-1}

$= 447.18 \times 10^{-3}$ A s

$= 447.18 \times 10^{-3}$ C

Now, the number of electron transferred is = 447.18×10^{-3} C / 1.602×10^{-19} C

$= 2.79 \times 10^{18}$

The surface-active Ni^{3+} sites participated in OER is = **2.79×10^{18}**

For AC-3

Calculated area associated with the reduction peak = 1.2256×10^{-3} V A

Hence the associated charge is = 1.2256×10^{-3} V A / 0.005 V s^{-1}

$= 245.12 \times 10^{-3}$ A s

$= 245.12 \times 10^{-3}$ C

Now, the number of electron transferred is = 245.12×10^{-3} C / 1.602×10^{-19} C

$= 1.53 \times 10^{18}$

The surface-active Ni^{3+} sites participated in OER is = **1.53×10^{18}**

Equation S2. Calculation of Turn over frequency (TOF) of different catalysts.

$$\mathbf{TOF = (j \times N_A) / (4 \times F \times n)}$$

Where,

j = current density at η = 300 mV

N_A = Avogadro number

F = Faraday constant

n = number of active Co-sites

For AC-2

TOF = $[(150 \times 10^{-3}) (6.023 \times 10^{23})] / [(96485) (4) (3.07 \times 10^{18})]$

TOF = 0.076 s^{-1}

For AC-1

TOF = $[(15.00 \times 10^{-3}) (6.023 \times 10^{23})] / [(96485) (4) (2.79 \times 10^{18})]$

TOF = 0.008 s^{-1}

For AC-3

TOF = $[(35.00 \times 10^{-3}) (6.023 \times 10^{23})] / [(96485) (4) (1.53 \times 10^{18})]$

TOF = 0.036 s^{-1}

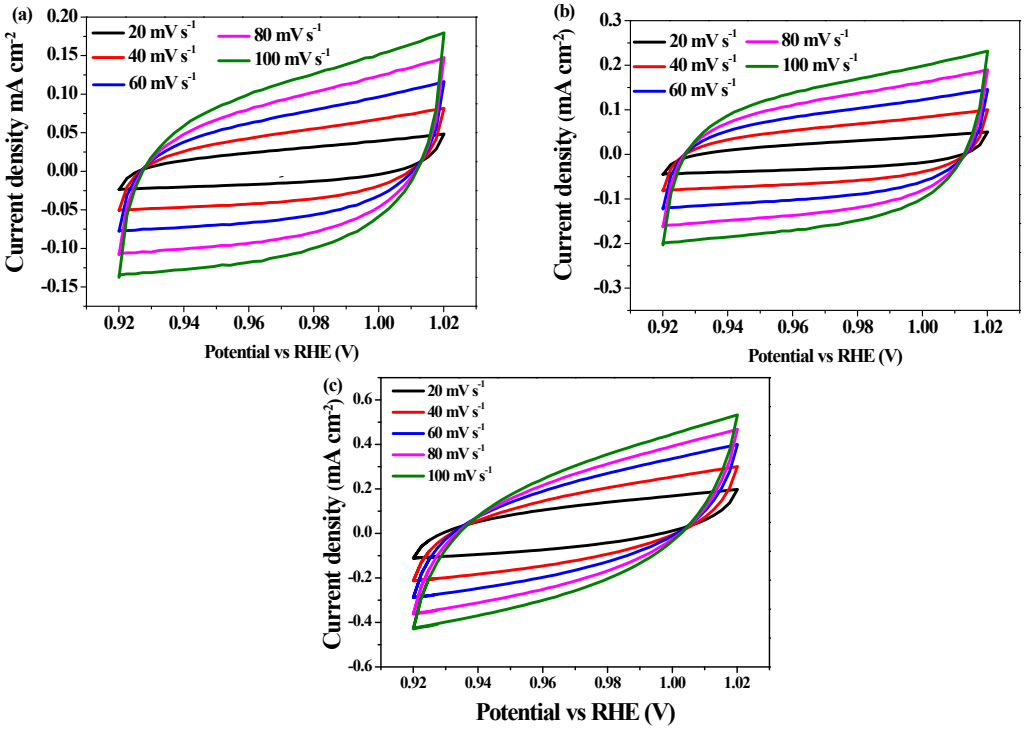

Figure S34. Electrochemical capacitance plot of (a) AC-1; (b) AC-3, and (c) AC-2 utilized for the determination of C_{dl}.

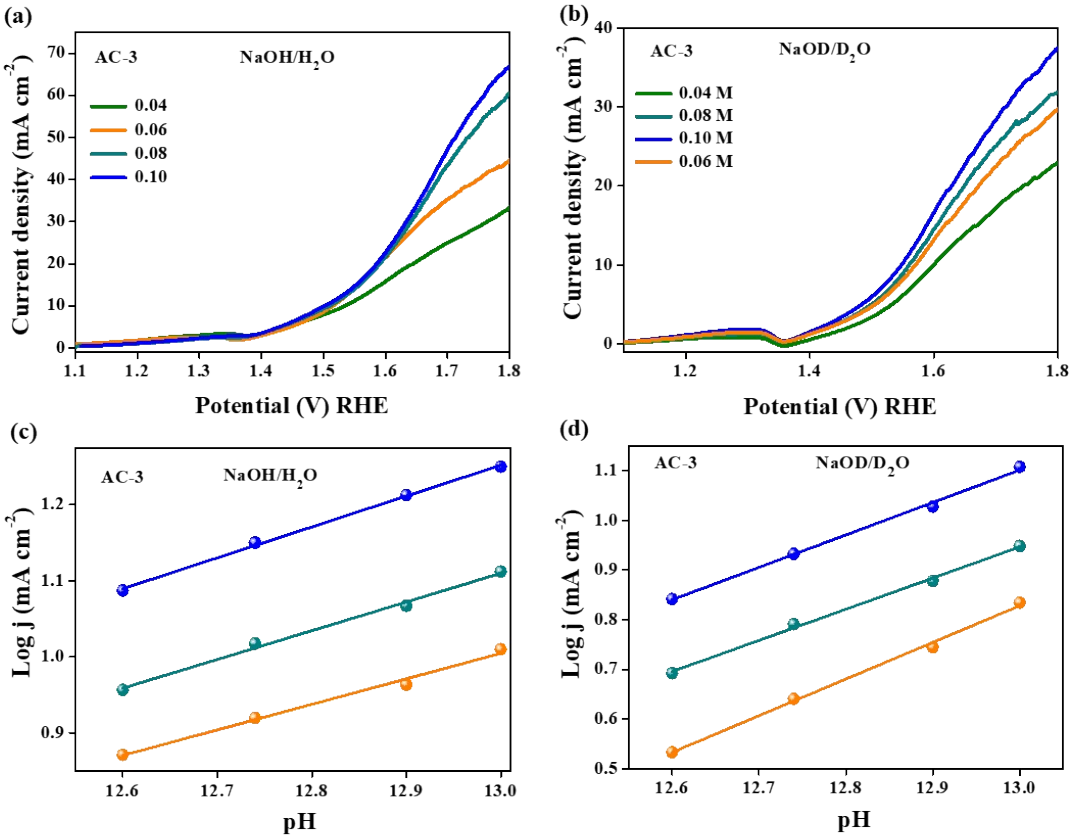

Figure S35. (a-b) LSV curves for OER in $NaOH/H_2O$ and $NaOD/D_2O$ at different pHs; (c-d) the pH-dependent kinetic study in $H_2O/NaOH$ and $D_2O/NaOD$.

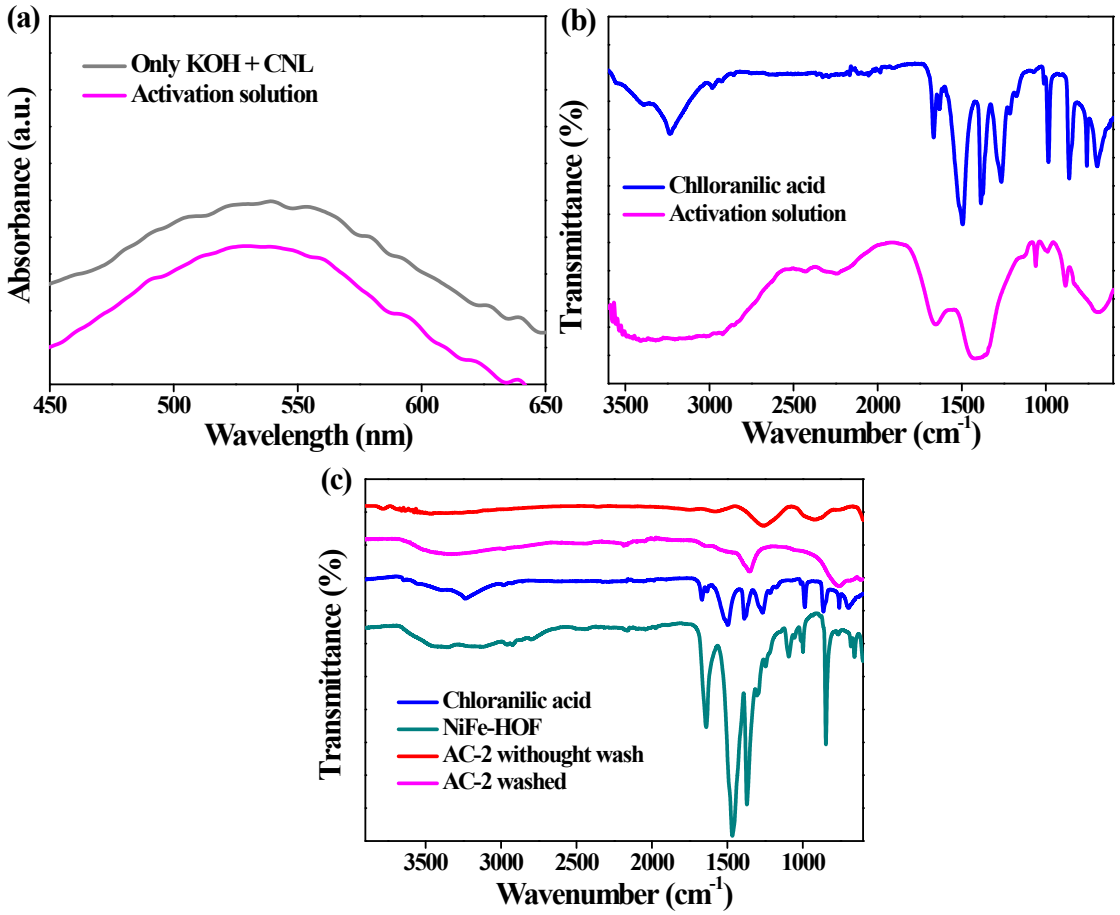

Figure S36. (a) UV-Visible spectra of the electrolyte solution after the activation of NiFe-HOF to AC-2 is compared with that of chloranilic acid in KOH solution. (b) IR spectra of free ligand (chloranilic acid) and the electrolyte solution after the activation of NiFe-HOF to AC-2. (c) IR spectra AC-2 without washing and after washing were compared with free ligand (chloranilic acid) NiFe-HOF. The peaks at 1665 cm^{-1} were assigned for the stretching vibrations of C=O group in chloranilic acid.[19,4]

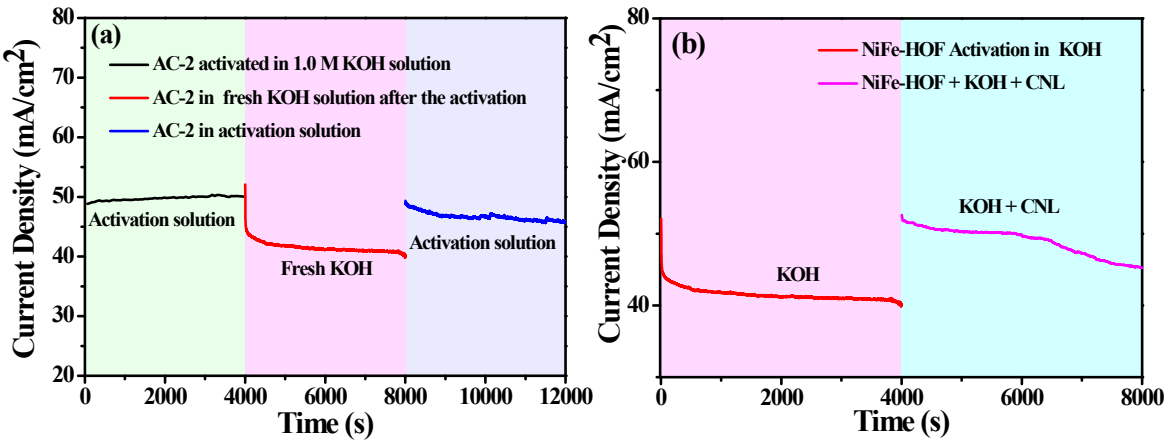

Figure S37. CA profiles of AC-2 in different electrolyte solutions. (a) NiFe-HOF was activated by CV in 1.0 M aqueous KOH solution to get AC-2 and CA was carried out with AC-2 in the same solution to attain a current density of ~ 50 mA/cm^2. Then AC-2 was removed from the activation solution, placed in fresh KOH solution, and CA was carried out. A decrease in the current density (~ 40 mA/cm^2) was observed. AC-2 further regained its activity when placed in the activation solution. (b) The effect of the addition of the fresh chloranilic acid in the KOH solution. A significant increase in the current density has been observed.

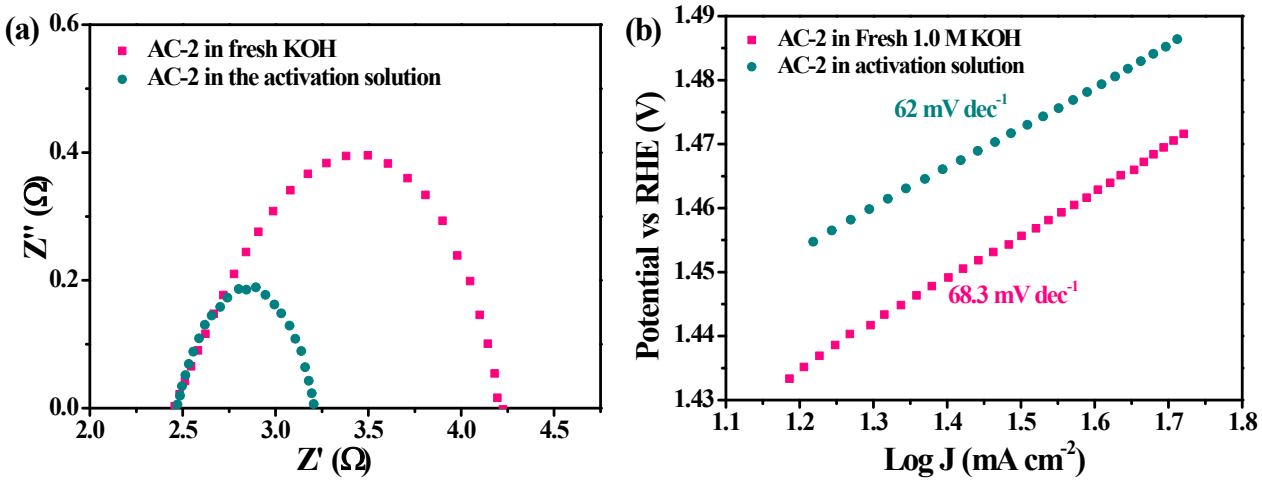

Figure S38. (a) EIS plots of AC-2 in activation solution and in fresh 1.0 M KOH solution. (b) Tafel plots of AC-2 in activation solution and in fresh 1.0 M KOH solution.

References

1 K. V Nielson, L. Zhang, Q. Zhang and T. L. Liu, *Inorg. Chem.*, 2019, **58**, 10756–10760.

2 M. E. Ziebel, J. C. Ondry and J. R. Long, *Chem. Sci.*, 2020, **11**, 6690–6700.

3 L. E. Darago, M. L. Aubrey, C. J. Yu, M. I. Gonzalez and J. R. Long, *J. Am. Chem. Soc.*, 2015, **137**, 15703–15711.

4 N. Biliskov, B. Kojic-Prodic, G. Mali, K. Molcanov, and J. Stare, *J. Phys. Chem. A*, 2011, **115**, 3154–3166.

5 K. Rui, G. Zhao, Y. Chen, Y. Lin, Q. Zhou, J. Chen, J. Zhu, W. Sun, W. Huang and S. X. Dou, *Adv. Funct. Mater.*, 2018, **28**, 1801554.

6. J. Duan, S. Chen, C. Zhao, *Nat. Commun.,* 2017, **8**, 15341.

7 J. Zhou, Z. Han, X. Wang, H. Gai, Z. Chen, T. Guo, X. Hou, L. Xu, X. Hu, M. Huang, S. V Levchenko and H. Jiang, *Adv. Funct. Mater.*, 2021, **31**, 2102066.

8 A. K. Singh, K. Bijalwan, N. Kaushal, A. Kumari, A. Saha and A. Indra, *ACS Appl. Nano Mater.,* 2023, **6**, 8036–8045.

9 Z. Li, X. Wu, X. Xiang B. Shen, Z. Teng, D. Sun, G. Fu, and Y. Tang, *Adv. Powder, Mater*., 2022, **01**, 100020

10 T. Li, Y. Hu, K. Liu, J. Yin, Y. Li, G. Fu, Y. Zhang, and Y. Tang, *J. Chem. Eng*., 2022, **427**, 131992.

11 S. Liu, H. Zhang, E. Hu, T. Zhu, C. Zhou, Y. Huang, M. Ling, X. Gao, and Z. Lin, *J. Mater. Chem. A,* 2021, **9**, 23697-23702.

12 B. Singh, O. Prakash, P. Maiti, P. W. Menezes and A. Indra, *Chem. Commun.*, 2020, **56**, 15036–15039.

13 X. Du, G. Ma, Y. Wang, X. Han, X. Zhang, *Dalton Trans.,* 2021, **50**, 14001–14008.

14 T. A. Kandiel, *Appl. Catal. A Gen.*, 2019, **586**, 117226.

15 J. M. Chen, Y. Y. Chin, M. Valldor, Z. Hu, J. M. Lee, S. C. Haw, N. Hiraoka, H. Ishii, C. W. Pao, K. D. Tsuei, J. F. Lee, H. J. Lin, L. Y. Jang, A. Tanaka, C. Te Chen and L. H. Tjeng, *J. Am. Chem. Soc.*, 2014, **136**, 1514–1519.

16 T. Burnus, Z. Hu, H. Wu, J. C. Cezar, S. Niitaka, H. Takagi, C. F. Chang, N. B. Brookes, H. J. Lin, L. Y. Jang, A. Tanaka, K. S. Liang, C. T. Chen and L. H. Tjeng, *Phys. Rev. B - Condens. Matter Mater. Phys.*, 2008, **77**, 205111.

17 N. Hollmann, Z. Hu, M. Valldor, A. Maignan, A. Tanaka, H. H. Hsieh, H. J. Lin, C. T. Chen and L. H. Tjeng, *Phys. Rev. B - Condens. Matter Mater. Phys.*, 2009, **80**, 085111.

18 L. Han, X. Y. Yu, X. W. Lou, *Adv. Mater.,* 2016, **28**, 4601–4605.

19 H. H. Zou, C. Z. Yuan, H. Y. Zou, T. Y. Cheang, S. J. Zhao, U. Y. Qazi, S. L. Zhong, L. Wang and A. W. Xu, *Catal. Sci., Technol.,* 2017, **7**, 1549–1555.

20 X. Xu, H. Liang, F. Ming, Z. Qi, Y. Xie and Z. Wang, *ACS Catal.,* 2017, **7**, 6394–6399.

21 B. Chen, Z. Yang, Q. Niu, H. Chang, G. Ma, Y. Zhu, Y. Xia, Y, *Electrochem. commun.,* 2018, **93**, 191–196.

22 Y. Feng, X. Y.Yu, and U. Paik, *Sci. Rep.,* 2016, **6** , 34004.

23 X. Y.Yu, Y. Feng, B. Guan, X. W. D. Lou, U. Paik, U. *Energy Environ. Sci.,* 2016, **9**, 1246–1250.

24 J. Nai, Y. Lu, X. Y. Yu, *J. Mater. Chem. A,* 2018, **6**, 21891–21895.

25 N. Cheng, Q. Liu, J. Tian, X. Sun, Y. He, S. Zhai and A. M. Asiri, A. M, *Int. J. Hydrogen Energy,* 2015, **40**, 9866–9871.

26 S. Battiato, M. Urso, S. Cosentino, A. L. Pellegrino, S. Mirabella, and A. Terrasi, *Nanomaterials* 2021, **11**, 3010.

27 G. Q. Han, Y. R. Liu,W. H. Hu, B. Dong, X. Li, X. Shang, Y. M. Chai, Y. Q. Liu and C. G. Liu, *Appl. Surf. Sci.,* 2015, **359**, 172–176.

28 C. Xia, Q. Jiang, C. Zhao, M. N. Hedhili and H. N. Alshareef, *Adv. Mater.,* 2016, **28**, 77–85.

29 G. Yilmaz, C. F. Tan, Y. F. Lim and G. W. Ho, *Adv. Energy Mater.,* 2019, **9**, 1802983.
30 X. Li, G. Q. Han, Y. R. Liu, B. Dong, W. H. Hu, X. Shang, Y. M. Chai and C.G. Liu, *ACS Appl. Mater. Interfaces,* 2016, **8** , 20057–20066.
31 Y. Lin, H. Wang, C. K. Peng, L. Bu,C. L. Chiang, K. Tian, Y. Zhao, J. Zhao, Y. G. Lin, J. M. Lee and L. Gao, *Small*, 2020, **16**, 2002426.
32 Q. Zhou, T-T. Li, J. Qian, W. Xu, Y. Hu and Y-Q. Zheng, *ACS Appl. Energy Mater.,* 2018, **1**, 1364−1373.
33 S. Anantharaj, K. Karthick, M. Venkatesh, T. V. S. V. Simha, A. S. Salunke, L. Ma, H. Liang and S. *Kundu, Nano Energy,* 2017, **39,** 30–43.
34 P. Li, X. Duan, Y. Kuang,Y. Li, G. Zhang, W. Liu and X. Sun, *Adv. Energy Mater.,* 2018, **8** (15), 1703341.
35 Q. Liu, Y. Wang and X. Lu, *Catalysts,* 2023, **13**, 586.
36 M. Gong, Y. Li, H.Wang, Y. Liang, J. Z. Wu, J. Zhou, J. Wang, T. Regier, F. Wei and H. A. Dai, *J. Am. Chem. Soc.,* 2013, **135**, 8452–8455.
37 S. Dutta, A. Indra, Y. Feng, T. Song and U. Paik, *ACS Appl. Mater. Interfaces*, 2017, **9**, 33766–33774.
38 S. Anantharaj, S. R. Ede, K. Karthick, S. Sam Sankar, K. Sangeetha, P. E. Karthik and S. Kundu, *Energy Environ. Sci.*, 2018, **11**, 744–771.
39 S. Anantharaj, S. R. Ede, K. Sakthikumar, K. Karthick, S. Mishra and S. Kundu, *ACS Catal.*, 2016, **6**, 8069–8097.